AGU ADVANCING EARTH AND SPACE SCIENCE

JGR Space Physics

RESEARCH ARTICLE
10.1029/2020JA028882

**Key Points:**

- Broadband electrostatic waves are observed in the electron diffusion region of magnetotail reconnection
- The parallel electric field of these waves have a bipolar or continuous steepening waveform
- The electron holes are oblate, where the perpendicular scale sizes are much greater than the parallel scales sizes

**Correspondence to:**
Q. Lu and R. Wang,
qmlu@ustc.edu.cn;
rswan@ustc.edu.cn

**Citation:**
Yu, X., Lu, Q., Wang, R., Huang, K., Gao, X., & Wang, S. (2021). MMS observations of broadband electrostatic waves in electron diffusion region of magnetotail reconnection. *Journal of Geophysical Research: Space Physics*, *126*, e2020JA028882. https://doi.org/10.1029/2020JA028882

Received 28 OCT 2020
Accepted 15 FEB 2021



# MMS Observations of Broadband Electrostatic Waves in Electron Diffusion Region of Magnetotail Reconnection

**Xiancai Yu[1,2,3], Quanming Lu[1,2,3], Rongsheng Wang[1,2,3], Kai Huang[1,2,3], Xinliang Gao[1,2,3], and Shui Wang[1,2]**

[1]Department of Geophysics and Planetary Science, CAS Key Laboratory of Geospace Environment, University of Science and Technology of China, Hefei, China, [2]CAS Center for Excellence in Comparative Planetology, Hefei, China, [3]Mengcheng National Geophysical Observatory, School of Earth and Space Sciences, University of Science and Technology of China, Hefei, China

**Abstract** In this study, the broadband electrostatic waves are observed in electron diffusion region (EDR). Detailed analysis has shown that the parallel electric field of these waves have a bipolar or continuous steepening waveform. The bipolar structures of the parallel electric field are usually accompanied by electron holes (EHs) in phase space. The parallel spatial scales $l_{\parallel}$ of EHs are ~3–5 $\lambda_D$ ($\lambda_D$ is the Debye length), and the perpendicular spatial scales $l_{\perp}$ are larger than ~18.6 $\lambda_D$. Therefore, the length ratios $l_{\perp}$ / $l_{\parallel}$ are larger than ~3.7–6.2, which means that the EHs have oblate shapes. Associated with these plasma waves, electron beams propagating away from the X-line have been observed. By performing a one-dimensional (1-D) electrostatic particle-in-cell simulation of the bump-on-tail instability, we reproduce two types of waveforms similar to those observed in the EDR during the different evolution stage of the instability, which implies that these electrostatic waves are generated by the bump-on-tail instabilities.

## 1. Introduction

Magnetic reconnection is an important physical process in space and laboratory plasmas, which transforms magnetic energy into plasma kinetic and thermal energy with a reconfiguration of magnetic topology (Lapenta et al., 2016; Q. M. Lu et al., 2013; Parker, 1957; Sweet, 1958; Vasyliunas et al., 1975; Wang & Lu, 2019). It is believed that the key processes, which drive magnetic reconnection, generally occur in a small-scale region called the diffusion region, which includes the ion diffusion region and electron diffusion region. In the ion diffusion region, ions are decoupled with the magnetic field and electrons still are frozen in the magnetic field. The decoupling of ions and electrons motion leads to the Hall effects. In the symmetry reconnection, typical manifestation of the Hall effects are quadrupolar structure of out-of-plane magnetic fields, and bipolar electric fields pointing toward the center of the current sheet at the edge of the ion diffusion region (Birn et al., 2001; Fu et al., 2006; Lu et al., 2010; Shay et al., 2001; Sonnerup, 1979; Wang et al., 2010). In the electron diffusion region (EDR), the electrons are no longer coupled with the magnetic field, and the reconnection electric field is balanced by the off-diagonal electron pressure term (Hesse et al., 1999; S. Lu et al., 2013; Pritchett et al., 2001; Vasyliunas, 1975).

Plasma waves have been always observed in the diffusion region of magnetic reconnection. They can cause particle scattering and diffusion, and are believed to be a possible source of anomalous resistivity (Cattell et al., 2002; Drake et al., 2003; Graham, Khotyaintsev, Vaivads et al., 2017; Huang et al., 2012; Huba et al., 1977; Vasko et al., 2017). The plasma waves in the separatrix region have been thoroughly studied by both satellite observations and particle-in-cell simulations. These waves include whistler waves (Deng & Matsumoto, 2001; Graham, Khotyaintsev, Norgren et al., 2016; Huang et al, 2016, 2017; Wilder et al., 2016), lower-hybrid waves (Graham, Vaivads et al., 2017; Vaivads, Khotyaintsev et al., 2004), Langmuir waves (Vaivads, André et al., 2004), and electron holes (Cattell et al., 2005; Fujimoto & Machida, 2006; Graham et al., 2015; Huang et al., 2014; Matsumoto et al., 2003). However, there are very few studies on plasma waves in the EDR until the launching of MMS in 2015. Taking the advantage of high-resolution measurements, plasma waves in the EDR of magnetic reconnection have been analyzed. Cao et al. (2017) identified large-amplitude whistler waves propagating away from the X-line in the EDR of magnetopause reconnection, which may be excited by the electron temperature anisotropy. Jiang et al. (2019) observed the upper hybrid waves in the EDR, and they were considered to be generated due to the agyrotropic crescent electron distributions. Li et al. (2020) found the electron Bernstein waves near the EDR, which also may be driven by electron crescent distributions. By performing three-dimensional (3-D) particle-in-cell (PIC) simulations of magnetic reconnection with a guide field, Drake et al. (2003) found the electrostatic waves generated by the Buneman instability in the EDR, and they thought that the waves can lead to strong electron scattering associated with anomalous resistivity. In this study, we examined in detail electrostatic waves in a magnetotail reconnection event, and identified broadband electrostatic waves in the EDR.

## 2. MMS Observations and Simulations

On July 11, 2017, MMS crossed the electron diffusion region in the magnetotail reconnection event at 22:34 UT, which was reported first by Torbert et al (2018). The MMS spacecraft was located at around (−21.6, 4.1, 3.8)$R_E$ in the Geocentric Solar Magnetospheric (GSM) coordinate system. The largest interspacecraft distance between satellite was ∼21 km ∼0.7$d_e$ (where $d_e = c / \omega_{pe}$ ∼30 km is the electron inertial length based on the minimum of electron density $n_e = 0.03$ cm$^{-3}$, $c$ is the speed of light, and $\omega_{pe}$ is the electron plasma frequency). Here, we mainly use the magnetic field data with 128 sample/s from the Fluxgate Magnetometers (Russell et al., 2016), and the electric field data with 8192 sample/s from the Electric field Double Probe (Ergun et al., 2016; Lindqvist et al., 2016). The plasma data is obtained from the Fast Plasma Instrument (Pollock et al., 2016) of MMS1, in which the time resolutions for the electrons and the ions are 30 and 150 ms, respectively. In order to investigate this crossing, the local boundary normal coordinates system is used where $L = (0.9482, -0.2551, -0.1893)$, $M = (0.1749, 0.9168, -0.3591)$, and $N = (0.2651, 0.3074, 0.9139)$ relative to the GSM coordinate system, which is determined by the Minimum variance analysis (Sonnerup & Scheible, 1998) of the electron velocity (Genestreti et al., 2018).

Figure 1 shows the overview of the magnetotail reconnection event, and the measurements by MMS1 are exhibited in the current sheet coordinate system. Most of the time, $B_L$ is negative (Figure 1b), and the satellite is in the southern part of the current sheet. Both $B_N$ and the ion bulk flow $V_{iL}$ change from negative values to positive values. Therefore, we can plot the trajectory of the satellite in Figure 1a, which crossed the ion diffusion region from the tailward to the earthward. From 22:34:02 UT to 22:34:05 UT, we can observe the enhancement of the electron bulk velocity in the out-of-plane direction $V_{eM}$ (Figure 1d), whose peak value is close to 20,000 km/s ∼ $V_{Ae}$, in which $V_{Ae} = B / \sqrt{\mu_0 n_e m_e}$ is the local electron Alfven velocity. At ∼22:34:02–22:34:05 UT, $-(V_e \times B)_L$ is deviated from the measured electric field $E_{\perp L}$ in Figure 1f, and it means the electrons are no longer coupled with the magnetic field. The energy dissipation $J \cdot \mathrm{E}'$ has significant enhancement (see Figure 1g, where $\mathrm{E}' = E + V_e \times B$ is the non-ideal electric field) and the magnetic field $B_L$ gradually tends to a minimum. Therefore, we can know that the satellite crosses the EDR during this time period. In the EDR, we can also find the existence of the electric field $E_N$ pointing to the center of the current sheet, and its peak value is up to ∼50 mV/m. The same reconnection event, as well as the identification of the EDR, has been described by Torbert et al. (2018), Nakamura et al. (2019), Hwang et al. (2019), and Jiang et al. (2019), and we will not go into more details.

In the EDR, we can also observe the existence of plasma waves during the time period 22:34:02–22:34:05 UT. These plasma waves have large electric fluctuations, while the magnetic fluctuations are negligible (Figures 1h–1i). Figures 2b–2d plot the parallel component ($E_\parallel$) and the two perpendicular components of the electric fields ($E_{\perp 1}$ and $E_{\perp 2}$) in magnetic field-aligned coordinates. The frequencies of the plasma waves during the time period ∼22:34:02.1–22:34:02.95 UT are around the upper hybrid frequency, which has been thoroughly analyzed by Burch et al. (2019) and Jiang et al. (2019). The waves are considered to be the upper hybrid waves, which is excited by the multiple electron crescent distributions. Here, in this study, we will analyze the other plasma waves during the time period ∼22:34:03.1–22:34:05 UT, which has not been analyzed before. The plasma waves have a broadband spectrum, and their uppermost frequency is about the local electron plasma frequency $f_{pe}$ ($f_{pe} \sim 1800$Hz, the red curve shown in Figure 2e), and their parallel component is much larger than the two perpendicular components. We filter the electric field data and analyze the direction of the wave vector $k$ of this emission by the minimum variance analysis (MVA) (Sonnerup & Scheible, 1998). The direction of the wave vector $k = [0.7593, -0.2388, -0.6054]$ GSM determined by MVA has an ambiguity of 180° with respect to the ambient magnetic field, which cannot be judged whether the electrostatic plasma waves propagate parallel or antiparallel to the magnetic field.

10.1029/2020JA028882

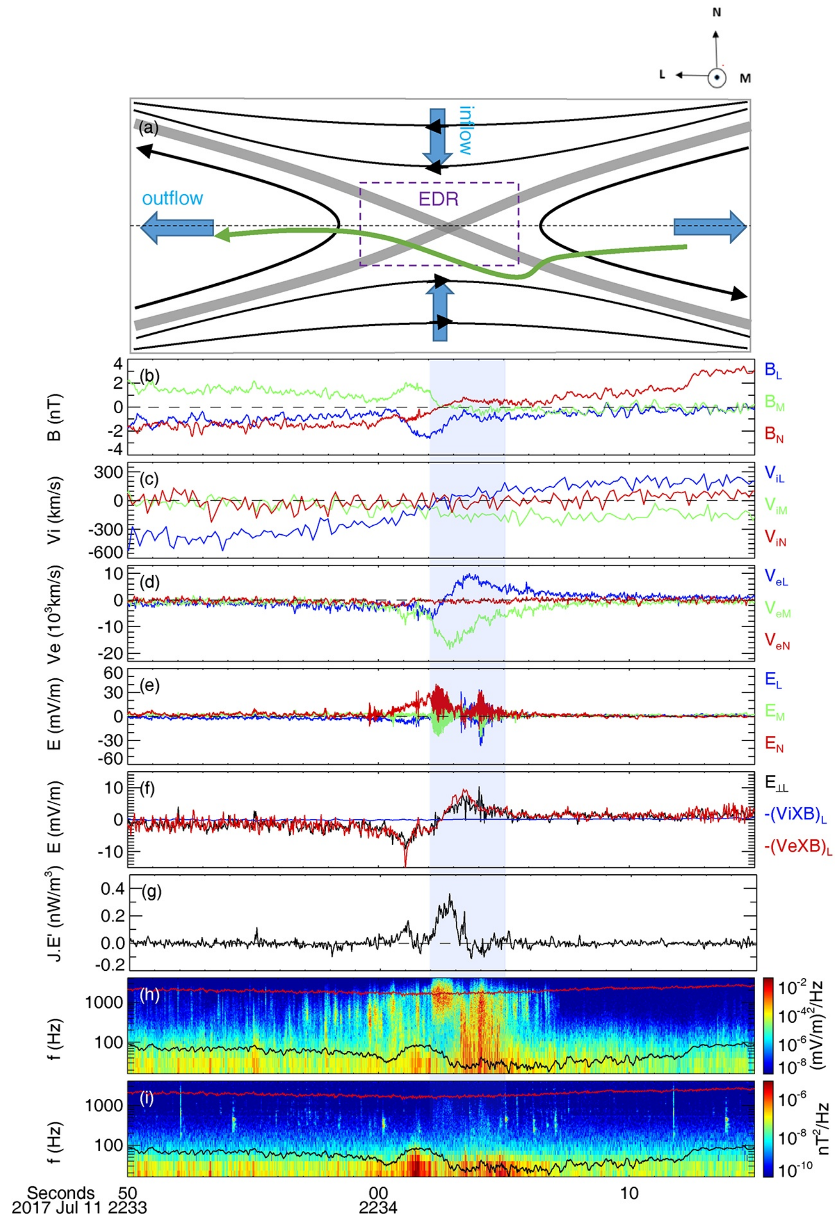

**Figure 1.** Overview of the electron diffusion regions (EDRs) encountered by MMS1 during 22:33:50-22:34:15UT. (a) A schematic illustrator of reconnection diffusion region. The green curve represents MMS trajectory, the purple area denotes the EDR. (b) Magnetic field vector. (c)–(d) Ion velocity and electron velocity. (e) Electric field vector. (f) The measured electric field $E_{\perp L}$, $-\left(V_i \times B\right)_L$ and $-\left(V_e \times B\right)_L$. (g) The energy dissipation $J \cdot E'$. (h)–(i) The power spectra of electric field and magnetic field, in which the red curves are the electron plasma frequency $f_{pe}$, and the black curves are the electron cyclotron frequency $f_{ce}$. The blue shaded area in the figure represents the EDR.

Figures 3A and 3B show the wave characteristics at two sub-periods (22:34:03.28–22:34:03.32 UT) and (22:34:04.05–22:34:04.09 UT). In the sub-period 22:34:03.28–22:34:03.32 UT, the parallel electric field $E_{||}$ has several bipolar structures, which is the typical characteristics of electron holes (EHs; Lu et al., 2008, 2005; Matsumoto et al., 2003; Omura et al., 1996; Wu et al., 2010), and the corresponding perpendicular electric field $E_{\perp 1}$ also has bipolar structure (Figure 3A2). Although the unipolar structures of the perpendicular electric field are more often observed in the EHs, the perpendicular electric field with a bipolar structure is also detected by satellite observations (Andersson et al., 2009; Matsumoto et al., 2003; Steinvall, Khotyaintsev, Graham, Vaivads, Contel, et al., 2019; Vasko et al., 2017; Wang et al, 2013, 2014). In Steinvall, Khotyaintsev,

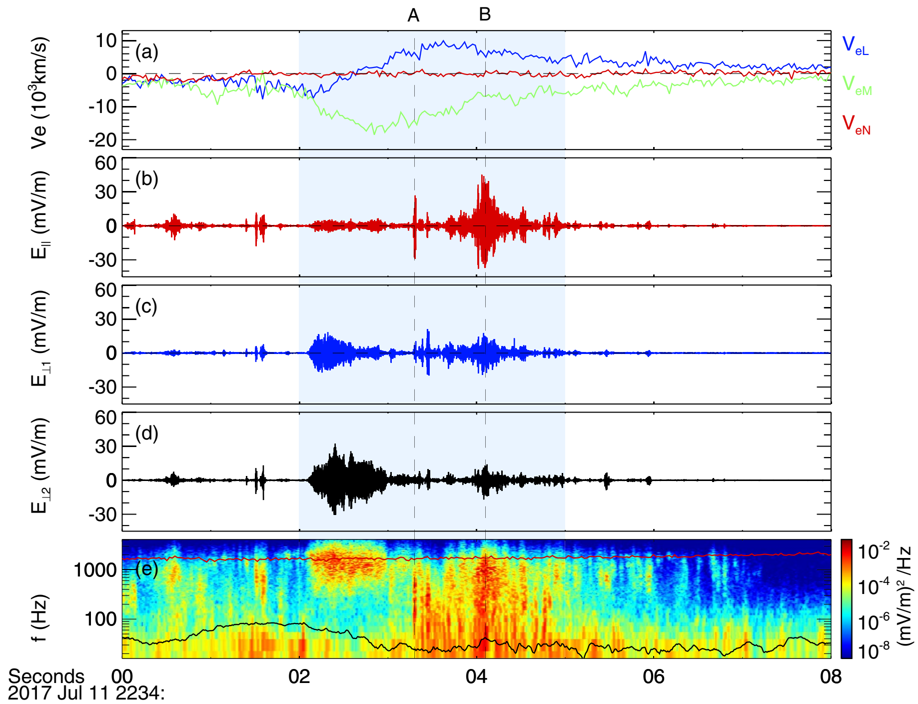


**Figure 2.** Electrostatic waves in the EDR. (a) Electron velocity. (b)–(d) Three components of high-frequency electric field in the field-aligned coordinate. (e) The power spectrum of electric field. The two vertical dashed lines represent the two sub-periods observed two different wave characteristics, marked by A and B.

Graham, Vaivads, Contel, et al. (2019), it is found that the perpendicular electric field with bipolar structure accounts for about 25% in 336 EHs. Therefore, it is not accidental to observe the bipolar $E_{\perp 1}$ in our event. However, the generation mechanism of this structure is still unknown. Figure 3B shows the waveform of the electric field during the sub-period 22:34:04.05–22:34:04.09 UT, corresponding to the largest intensity of the broadband electrostatic waves (Figure 2e). The electric field exhibits continuous steepening waveform. Its amplitude of the parallel component is ~40 mV/m, and the two perpendicular components are much smaller.

In this study, a train of EHs are observed by MMS 4, 2, and 1 successively (Figure 4d). Combining the above MVA of electric field and the satellite position (Figures 4a–4c), it can be determined that the EHs are propagating away from the X-line. We can use the time delay analysis to determine these EHs' parallel

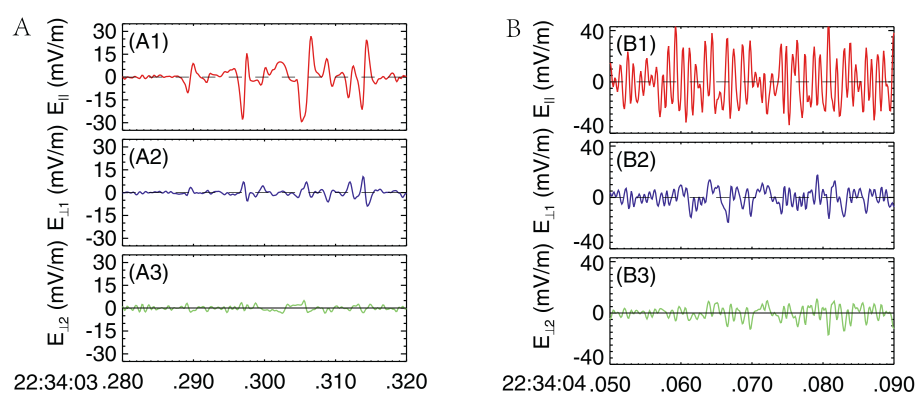


**Figure 3.** (A) and (B) show the wave characteristics at sub-period A (22:34:03.28–22:34:03.32 UT) and sub-period B (22:34:04.05–22:34:04.09 UT). (A1–A3) The measured electric field in the field-aligned coordinate at the sub-period A. (B1–B3) The measured electric field in the field-aligned coordinate at the sub-period B.

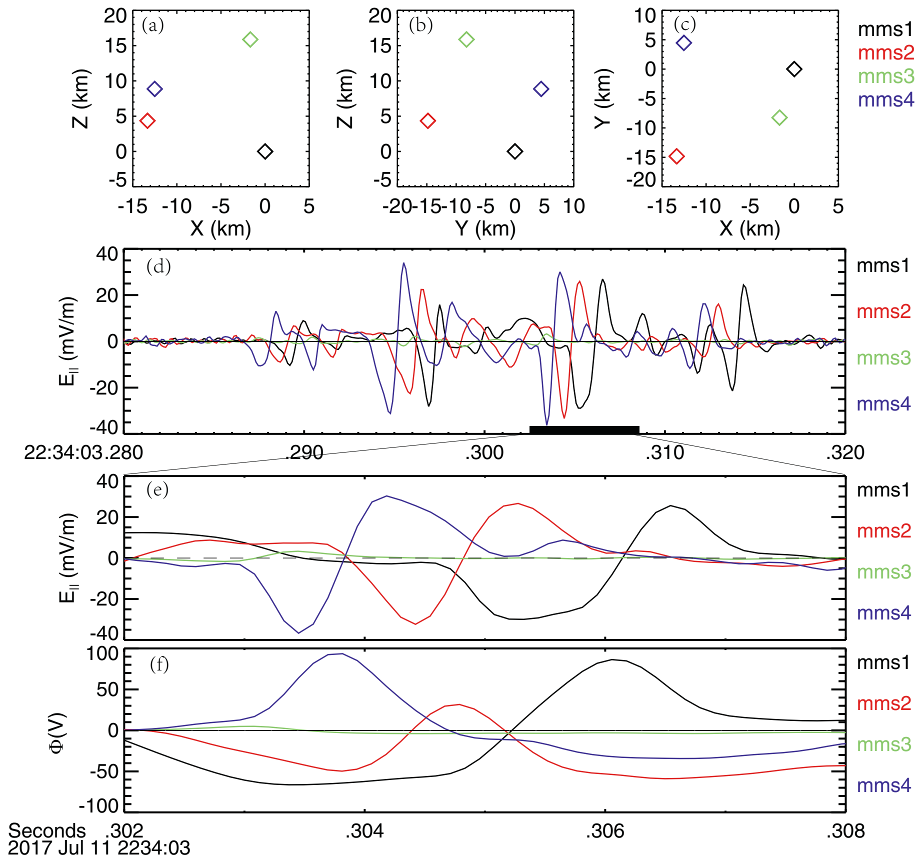


**Figure 4.** The time delay analysis of electron holes. (a)–(c) The spacecraft orientation in the field-aligned coordinates, where $z$ is parallel to B, the $y$ direction is defined as the vector product of $z$ and the vector pointing from the Earth to the Sun, which corresponds to the $x$ direction of geocentric solar ecliptic (GSE) coordinates, and the remaining component ($x$) is defined to complete an orthogonal right-handed coordinate system. (d) The parallel electric field $E_{\parallel}$ for a train of EHs observed by all four spacecraft. (e) Zoom-in on $E_{\parallel}$ for one particular EH. (f) The electric potential corresponding to $E_{\parallel}$ and $V_{\parallel}$.

propagation velocities (Holmes et al., 2018; Steinvall, Khotyaintsev, Graham, Vaivads, Lindqvist et al., 2019; Tong et al., 2018). For each EH, we can determine the time delay $\delta t_i$ of the bipolar $E_{\parallel}$ signal between every pair of spacecraft with the largest correlation coefficient $C_i$. The corresponding propagation velocity is $V_{\parallel i} = \Delta_i / \delta t_i$, where $\Delta_i$ is the spacecraft separation along $B$. Therefore the final parallel propagation velocity of the EH is $V_{\parallel} = \sum_{i=1}^{3} V_{\parallel i} C_i \Delta_i / \sum_{i=1}^{3} C_i \Delta_i$. The spatial scales in parallel direction $l_{\parallel}$ can be calculated by $l_{\parallel} = V_{\parallel}\overline{\tau}$, where $\overline{\tau}$ is the mean peak-to-peak time of the EH. According to the above method, the parallel propagation velocities of these EHs $V_{\parallel}$ are estimated to be ~−4,000–−6,000 km/s in the spacecraft frame, and the parallel spatial scales $l_{\parallel}$ are estimated to be ~2.8–4.8 km, i.e., ~3–5 $\lambda_D$ (where $\lambda_D = \left(\varepsilon_0 k_B T_e / n_e e^2\right)^{1/2}$ ~ 968m is the Debye length based on the electron density $n_e = 0.05$ cm$^{-3}$). From Figures 4b and 4c, the largest satellite separation in perpendicular direction is ~ 18 km, therefore, the perpendicular spatial scales $l_{\perp}$ are greater than or equal to ~18 km–18.6$\lambda_D$. In Figure 4f, we calculate the electric potential Φ according to the observed $E_{\parallel}$ (Figure 4e) as $\Phi = \int E_{\parallel} \cdot V_{\parallel} dt$. Here, MMS 4 observes the largest peak potential, Φ = ~100 V.

Figure 5 shows the electron phase-space density $f_e\left(v_{\parallel}\right)$ verses electron velocity $v_{\parallel}$ measured by MMS2 at two sub-periods, in which the rhombuses are the observations, and the red lines show the fitting result. In this region, the spacecraft potential is ~45 V (not shown), and the electron distributions has removed the influence of the spacecraft potential in Figure 5. From the MMS2 observations, the electron beams propagating away from the X-line ($\theta = 180^{\circ}$) are found near velocity $v_{e,b}$ ~ 14,000 − 20,000 km/s in both sub-periods. Based on the observations, we model these electron distributions with three bi-Maxwellians. When the EHs

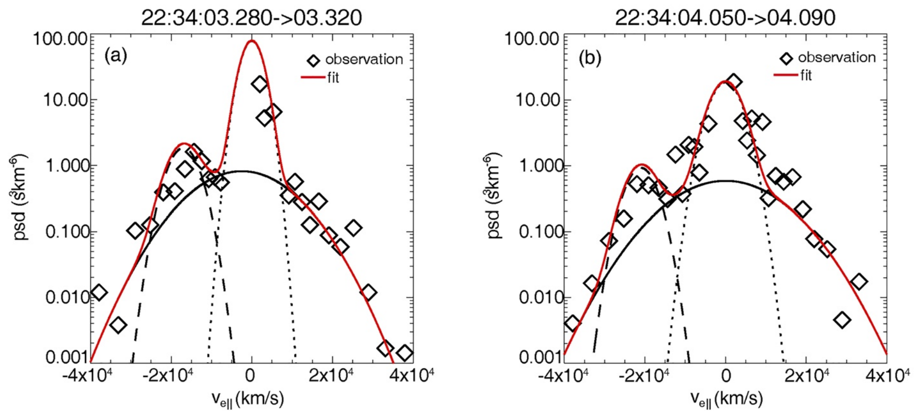


**Figure 5.** The electron distributions at two sub-periods. (a) The electron distribution in the 22:34:03.28–22:34:03.32 UT. (b) The electron distribution in the 22:34:04.05–22:34:04.09 UT. The rhombuses are the observations, and the red lines show the fitted result. The black dotted lines are the fitted cold electron distribution, the black solid lines represent the fitted hot electron distribution, and the black dashed lines are the fitted beam electron distribution.

are observed in the 22:34:03.28–22:34:03.32 UT, the electron distribution (shown in Figure 5a) includes cold (black dotted line), hot electrons (black solid line), and beam electrons (black dashed line). The density of the cold, hot, and beam electrons are $n_{e,c} = 0.015\ \mathrm{cm}^{-3}$, $n_{e,h} = 0.014\ \mathrm{cm}^{-3}$, and $n_{e,b} = 0.001\ \mathrm{cm}^{-3}$, and their temperatures are $T_{e,c} = 30$ eV, $T_{e,h} = 600$ eV, and $T_{e,b} = 60$ eV. The drift speeds of the hot electrons and the beam electrons are $v_{d,h} = -2{,}500$km/s and $v_{d,b} = -17{,}000$km/s. During the 22:34:04.05–22:34:04.09 UT, the electron distribution (shown in Figure 5b) also includes the cold (black dotted line), hot (black solid line) and beam electrons (black dashed line).

The EHs can be generated by the bump-on-tail instability, electron bi-stream instability, Buneman instability, and so on (Buneman, 1959; Graham, Khotyaintsev et al., 2016; Omura et al., 1996). In general, the EHs excited by the Buneman instability have propagation speed $\left(m_e / m_i\right)^{1/3} v_{e,b} \sim 0.08 v_{e,b} \sim 1388$ km/s (where $v_{e,b} = 17{,}000$ km/sis the beam velocity), which is much smaller than the observed EHs speed (4,000–6,000 km/s) in the observations. Therefore, the Buneman instability can be excluded. The electron bi-stream instability cannot generate the EHs when the beam density is much less than the density of the ambient plasma. Form Figure 5a, the density ratio is $n_{e,b} / n_e \sim 0.03$, in which $n_e = n_{e,c} + n_{e,h} + n_{e,b}$ is the total electron density, thus these EHs cannot be generated by the electron bi-stream instability in our observations. Based on the extracted parameters for the cold, hot and beam electrons from observations, the estimated phase velocity at maximum growth rate based on the linear theory analysis is about $V_{ph}$~14,000 km/s, which is close to the beam velocity $v_{e,b} = 17{,}000$km/s. Although there are cold electrons, due to the thermal effect of hot electrons is large enough, cold electrons and hot electrons can be regarded as one electron population with thermal effect, which can interact with beam electrons to excite the EHs. Hence, we think that these EHs are generated by the bump-on-tail instability. In the observation, the EHs speed obtained by multi-spacecraft timing analysis is $\sim 0.4 V_{ph}$, which has a deviation from the linear theory analysis, but the difference may be caused due to three-dimensional structure of the EHs in reality (Figure 3).

In order to prove that these electrostatic plasma waves are generated by the bump-on-tail instability, we perform one-dimensional (1-D) electrostatic particle simulations based on the observations. Periodic boundary conditions are used in the simulations, and the waves are assumed to propagate along the $x$ direction. The ions are motionless, and their effects on the plasma waves are neglected. Three different electron components from the observations are employed: cold electrons, hot electrons, and beam electrons, and their number densities are represented by $n_c$, $n_h$, and $n_b$. The thermal velocity of hot electrons is $v_{te}$ (where $v_{te} = \sqrt{2k_B T_e / m_e}$, and $T_e$ is the temperature of hot electrons), and the drift velocity of hot electrons is $v_{d\_h} = -0.15 v_{te}$. The thermal velocity of cold electrons is $0.15 v_{te}$, and there is no the drift velocity for cold electrons. The thermal velocity of beam electrons is $0.15 v_{te}$, and the drift velocity of beam electrons is

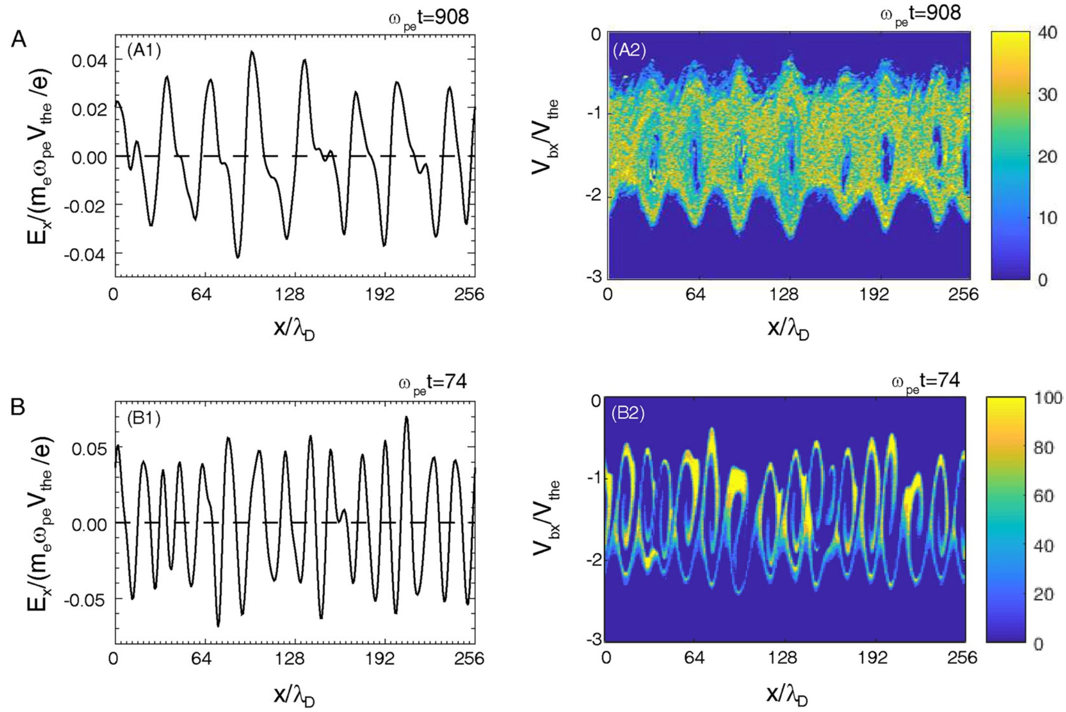


**Figure 6.** The results of 1D electrostatic particle simulations. (A1) and(B1) The electric field $E_x$ at $\omega_{pe}t = 908$ and $\omega_{pe}t = 74$. (A2) and (B2) The $x - v_{bx}$ phase diagram of electron beams at $\omega_{pe}t = 908$ and $\omega_{pe}t = 74$.

$v_{d\_b} = -1.8v_{te}$. The time step is chosen as $\Delta t = 0.02\omega_{pe}^{-1}$ (where $\omega_{pe} = \left(n_0e^2 / m_e\varepsilon_0\right)^{1/2}$ is the electron plasma frequency, and $n_0 = n_c + n_h + n_b$). The grid size is $\lambda_D$ (where $\lambda_D = \left(\varepsilon_0 k_B T_e / n_c e^2\right)^{1/2}$ is the Debye length), and there are 256 grid cells. The average number of the particles in a cell is 900. The density of cold electrons is equivalent to that of the hot electrons, and the density ratio is $n_b / n_0 = 0.05$. Figure 6(A1) and Figure 6(B1) plot the electric field $E_x$ (parallel to **B**) at $\omega_{pe}t = 908$ and $\omega_{pe}t = 74$ for this case. The waveforms of electrostatic wave emissions as a function of time shown in Figure 3(A1) and Figure 3(B1) are similar to those found in simulations as a function of time (Figure 6(A1) and Figure 6(B1)). Figure 6(A2) and Figure 6(B2) show the $x - v_{bx}$ phase diagram of electrons at $\omega_{pe}t = 908$ and $\omega_{pe}t = 74$, which shows formation of electron holes through coalescence of the vortices of trapped electrons. Therefore, the different waveforms of electrostatic plasma waves observed by spacecraft may be the results of different stage during the time evolution of the electron bump-on-tail instability.

We also change density of cold electrons ($n_c / n_0$ =0.3, 0.05, and 0), and find that the bipolar and continuous steepening waveforms still exist in these simulations (not shown). The linear theory analysis for different density of cold electrons shows that the growth rate changes little and the phase velocity is almost the same. Therefore, combining simulations and linear theory analysis, we think that the cold electrons are not critical for the formation of the bipolar and continuous steepening waveforms.

## 3. Discussion and Conclusions

In this study, we analyzed the electrostatic plasma waves in the EDR observed by MMS in the magnetotail reconnection event on July 11, 2017. Besides the upper hybrid waves, which have been thoroughly studied by Torbert et al. (2018), Burch et al. (2019), and Jiang et al., (2019), for the first time, we found that there still exist another type of electrostatic plasma waves with a broadband spectrum. In these waves, we found two different waveforms of the parallel electric field $E_{\parallel}$ at two sub-periods. At 22:34:03.28–22:34:03.32 UT, the $E_{\parallel}$ had a train of bipolar structures, which is typical characteristic of EHs. At 22:34:04.05–22:34:04.09 UT, the waveforms of the parallel electric field were continuous steepening. From the detailed analysis of the electron distribution, electron beams propagating away from the X-line have been observed when these electrostatic waves were observed. At the same time, the cold and hot electrons were also observed at two sub-periods. Based on the linear theory analysis, we thought that these EHs are generated by the electron bump-on-tail instability. Combining to the results of the 1-D electrostatic PIC, we thought that these different waveforms of electrostatic plasma waves may be the results at different stages during the time evolution of the bump-on-tail instability.

The analysis of 3-D configuration of the electron holes is a subject of concern, which can be valuable for analysis of electron holes observed in space plasmas. In this study, the parallel spatial scales $l_{\parallel}$ of the EHs were ~3–5 $\lambda_D$, and the perpendicular spatial scales $l_{\perp}$ were greater than or equal to ~18.6 $\lambda_D$. The length ratios $l_{\perp}$ / $l_{\parallel}$ were greater than or equal to ~3.7–6.2, which means that the EHs are oblate shapes conforming to the previous observations and simulations (Franz et al., 2000, 2005; Holmes et al., 2018; Steinvall, Khotyaintsev, Graham, Vaivads, Lindqvist et al., 2019; Tong et al., 2018).

It is generally accepted that broadband electrostatic waves play an important role in plasma dynamics (Che et al., 2010; Drake et al., 2003; Goldman et al., 2014; Khotyaintsev et al., 2010; Mozer et al., 2015; Vasko et al., 2017). Khotyaintsev et al. (2010) present the observations of electric solitary structures inside a magnetic flux rope close to a magnetic reconnection region, they found that the electric solitary structures provide a way for the dynamic reconnecting current sheet to dissipate energy, and can be very important for electron and ion energization. With particle-in-cell simulations, Drake et al. (2003) found that electrostatic solitary structures can efficiently scatter electrons in the EDR, thereby contributing to anomalous dissipation processes. In addition, Goldman et al. (2014) shown that electrostatic solitary structures can Cherenkov radiate whistler waves which in turn affect the reconnection rate in the simulations of magnetic reconnection. Therefore, the broadband electrostatic waves observed in the EDR may change the reconnection rate, and energize electrons more efficiently. However, the period of time observed the broadband electrostatic waves is too short (~30 ms) in our event, there is no detailed particle data to support us to analyze their characteristics, which is beyond the scope of the study.

Because of the reduced separations between characteristic electron scales, such as the Debye length and electron inertial length, the dynamic properties of the electron diffusion region during magnetic reconnection has been difficult to study by simulations, and even high-frequency plasma waves are suppressed. However, our observations have shown that the electron diffusion region may be intrinsic to the excitation of high-frequency electrostatic waves.

## Data Availability Statement

All the MMS data used in this work are available at the MMS data center (https://lasp.colorado.edu/mms/sdc/). The authors acknowledge for the data resources from "National Space Science Data Center, National Science & Technology Infrastructure of China" (http://www.nssdc.ac.cn). The simulation results are generated from our computer simulation model, which is described in Section 2. The simulation data used to plot the figures in this study can be downloaded from https://dx.doi.org/10.12176/01.99.00260.

**Acknowledgments**
This work was supported by the Strategic Priority Research Program of Chinese Academy of Sciences, Grant no. XDB 41000000, the NSFC Grant 41527804, 41774169, 41922030, and Key Research Program of Frontier Sciences, CAS (QYZDJ-SSW-DQC010).

## References

Andersson, L., Ergun, R. E., Tao, J., Roux, A., LeContel, O., Angelopoulos, V., et al. (2009). New features of electron phase space holes observed by the THEMIS mission. *Physical Review Letters*, *103*, 05990. https://doi.org/10.1103/PhysRevLett.103.059901

Birn, J., Drake, J. F., Shay, M. A., Rogers, B. N., Denton, R. E., Hesse, M., et al. (2001). Geospace environmental modeling (GEM) magnetic reconnection challenge. *Journal of Geophysical Research*, *106*(A3), 3715–3719. https://doi.org/10.1029/1999JA900449

Buneman, O. (1959). Dissipation of currents in ionized media. *Physical Review*, *115*, 503–517. https://doi.org/10.1103/PhysRev.115.503

Burch, J. L., Dokgo, K., Hwang, K. J., Torbert, R. B., Graham, D. B., Webster, J. M., et al. (2019). High-frequency wave generation in magnetotail reconnection: Linear dispersion analysis. *Geophysical Research Letters*, *46*, 4089–4097. https://doi.org/10.1029/2019GL082471

Cao, D., Fu, H. S., Cao, J. B., Wang, T. Y., Graham, D. B., Chen, Z. Z., et al. (2017). MMS observations of whistler waves in electron diffusion region. *Geophysical Research Letters*, *44*, 3954–3962. https://doi.org/10.1002/2017GL072703

Cattell, C., Crumley, J., Dombeck, J., Wygant, J., & Mozer, F. S. (2002). Polar observations of solitary waves at the Earth's magnetopause. *Geophysical Research Letters*, *29*(5), 1065. https://doi.org/10.1029/2001GL014046

Cattell, C., Dombeck, J., Wygant, J., Drake, J. F., Swisdak, M., Goldstein, M. L., et al. (2005). Cluster observations of electron holes in association with magnetotail reconnection and comparison to simulations. *Journal of Geophysical Research*, *110*, A01211. https://doi.org/10.1029/2004JA010519

Che, H., Drake, J. F., Swisdak, M., & Yoon, P. H. (2010). Electron holes and heating in the reconnection dissipation region. *Geophysical Research Letters*, *37*, L11105. https://doi.org/10.1029/2010GL043608

Deng, X. H., & Matsumoto, H. (2001). Rapid magnetic reconnection in the Earth's magnetosphere mediated by whistler waves. *Nature*, *410*(6828), 557–560. https://doi.org/10.1038/35069018

Drake, J., Swisdak, M., Cattell, C., Shay, M., Rogers, B., & Zeiler, A. (2003). Formation of electron holes and particle energization during magnetic reconnection. *Science*, *299*, 873–877. https://doi.org/10.1126/science.1080333

Ergun, R. E., Tucker, S., Westfall, J., Goodrich, K. A., Malaspina, D. M., Summers, D., et al. (2016). The axial double probe and fields signal processing for the MMS mission. *Space Science Reviews*, *199*(1–4), 167–188. https://doi.org/10.1007/s11214-014-0115-x

Franz, J. R., Kintner, P. M., Pickett, J. S., & Chen, L.-J. (2005). Properties of small-amplitude electron phase-space holes observed by Polar. *Journal of Geophysical Research*, *110*, A09212. https://doi.org/10.1029/2005JA011095

Franz, J. R., Kintner, P. M., Seyler, C. E., Pickett, J. S., & Scudder, J. D. (2000). On the perpendicular scale of electron phase-space holes. *Geophysical Research Letters*, *27*(2), 169–172. https://doi.org/10.1029/1999GL010733

Fu, X. R., Lu, Q. M., & Wang, S. (2006). The process of electron acceleration during collisionless magnetic reconnection. *Physics of Plasmas*, *13*, 012309. https://doi.org/10.1063/1.2164808

Fujimoto, K., & Machida, S. (2006). A generation mechanism of electrostatic waves and subsequent electron heating in the plasma sheet-lobe boundary region during magnetic reconnection. *Journal of Geophysical Research*, *111*, A09216. https://doi.org/10.1029/2005JA011542

Genestreti, K. J., Nakamura, T. K. M., Nakamura, R., Denton, R. E., Torbert, R. B., Burch, J. L., et al. (2018). How accurately can we measure the reconnection rate EM for the MMS diffusion region event of 11 July 2017? *Journal of Geophysical Research: Space Physics*, *123*, 9130–9149. https://doi.org/10.1029/2018JA025711

Goldman, M. V., Newman, D. L., Lapenta, G., Andersson, L., Gosling, J. T., Eriksson, S., et al. (2014). Čerenkov emission of quasiparallel whistlers by fast electron phase-space holes during magnetic reconnection. *Physical Review Letters*, *112*, 145002. https://doi.org/10.1103/PhysRevLett.112.145002

Graham, D. B., Khotyaintsev, Y. V., Norgren, C., Vaivads, A., André, M., Toledo-Redondo, S., et al. (2017). Lower hybrid waves in the ion diffusion and magnetospheric inflow regions. *Journal of Geophysical Research: Space Physics*, *122*, 517–533. https://doi.org/10.1002/2016JA023572

Graham, D. B., Khotyaintsev, Y. V., Vaivads, A., & André, M. (2015). Electrostatic solitary waves with distinct speeds associated with asymmetric reconnection. *Geophysical Research Letters*, *42*, 215–224. https://doi.org/10.1002/2014GL062538

Graham, D. B., Khotyaintsev, Y. V., Vaivads, A., & André, M. (2016). Electrostatic solitary waves and electrostatic waves at the magnetopause. *Journal of Geophysical Research: Space Physics*, *121*, 3069–3092. https://doi.org/10.1002/2015JA021527

Graham, D. B., Khotyaintsev, Y. V., Vaivads, A., Norgren, C., André, M., Webster, J. M., et al. (2017). Instability of agyrotropic electron beams near the electron diffusion region. *Physical Review Letters*, *119*(2), 025101. https://doi.org/10.1103/PhysRevLett.119.025101

Graham, D. B., Vaivads, A., Khotyaintsev, Y. V., & André, M. (2016). Whistler emission in the separatrix regions of asymmetric magnetic reconnection. *Journal of Geophysical Research: Space Physics*, *121*, 1934–1954. https://doi.org/10.1002/2015JA021239

Hesse, M., Schindler, K., Birn, J., & Kuznetsova, M. (1999). The diffusion region in collisionless magnetic reconnection. *Physics of Plasmas*, *6*(5), 1781–1795. https://doi.org/10.1063/1.873436

Holmes, J. C., Ergun, R. E., Newman, D. L., Ahmadi, N., Andersson, L., LeContel, O., et al. (2018). Electron phase-space holes in three dimensions: Multispacecraft observations by magnetospheric multiscale. *Journal of Geophysical Research: Space Physics*, *123*, 9963–9978. https://doi.org/10.1029/2018JA025750

Huang, C., Lu, Q., Wang, P., Wu, M., & Wang, S. (2014). Characteristics of electron holes generated in the separatrix region during antiparallel magnetic reconnection. *Journal of Geophysical Research: Space Physics*, *119*(8), 6445–6454. https://doi.org/10.1002/2014JA019991

Huang, S. Y., Fu, H. S., Yuan, Z. G., Vaivads, A., Khotyaintsev, Y. V., Retino, A., et al. (2016). Two types of whistler waves in the hall reconnection region. *Journal of Geophysical Research: Space Physics*, *121*(7), 6639–6646. https://doi.org/10.1002/2016ja022650

Huang, S. Y., Yuan, Z. G., Sahraoui, F., Fu, H. S., Pang, Y., Zhou, M., et al. (2017). Occurrence rate of whistler waves in the magnetotail reconnection region. *Journal of Geophysical Research: Space Physics*, *122*, 7188–7196. https://doi.org/10.1002/2016JA023670

Huang, S. Y., Zhou, M., Sahraoui, F., Vaivads, A., Deng, X. H., André, M., et al. (2012). Observations of turbulence within reconnection jet in the presence of guide field. *Geophysical Research Letters*, *39*, L11104. https://doi.org/10.1029/2012GL052210

Huba, J. D., Gladd, N. T., & Papadopoulos, K. (1977). The lower-hybrid-drift instability as a source of anomalous resistivity for magnetic field line reconnection. *Geophysical Research Letters*, *4*(3), 125–128. https://doi.org/10.1029/gl004i003p00125

Hwang, K.-J., Choi, E., Dokgo, K., Burch, J. L., Sibeck, D. G., Giles, B. L., et al. (2019). Electron vorticity indicative of the electron diffusion region of magnetic reconnection. *Geophysical Research Letters*, *46*, 6287–6296. https://doi.org/10.1029/2019GL082710

Jiang, K., Huang, S. Y., Yuan, Z. G., Sahraoui, F., Deng, X. H., Yu, X. D., et al. (2019). The role of upper hybrid waves in the magnetotail reconnection electron diffusion region. *The Astrophysical Journal Letters*, *881*(2), L28. https://doi.org/10.3847/2041-8213/ab36b9

Khotyaintsev, Y. V., Vaivads, A., Andre, M., Fujimoto, M., Retino, A., & Owen, C. J. (2010). Observations of slow electron holes at a magnetic reconnection site. *Physical Review Letters*, *105*(16), 165002. https://doi.org/10.1103/PhysRevLett.105.165002

Lapenta, G., Wang, R., & Cazzola, E. (2016). Reconnection separatrix: Simulations and spacecraft measurements. In W. Gonzalez, & E. Parker (Eds.), *Magnetic reconnection: Concepts and applications* (pp. 315–344). Springer. https://doi.org/10.1007/978-3-319-26432-5_8

Li, W. Y., Graham, D. B., Khotyaintsev, Y. V., Vaivads, A., André, M., Min, K., et al. (2020). Electron Bernstein waves driven by electron crescents near the electron diffusion region. *Nature Communications*, *11*(1), 141.

Lindqvist, P.-A., Olsson, G., Torbert, R. B., King, B., Granoff, M., Rau, D., et al. (2016). The spin-plane double probe electric field instrument for MMS. *Space Science Reviews*, *199*(1–4), 137–165. https://doi.org/10.1007/s11214-014-0116-9

Lu, Q. M., Huang, C., Xie, J., Wang, R., Wu, M., Vaivads, A., & Wang, S. (2010). Features of separatrix regions in magnetic reconnection: Comparison of 2-D particle-in-cell simulations and Cluster observations. *Journal of Geophysical Research*, *115*, A11208. https://doi.org/10.1029/2010JA015713

Lu, Q. M., Lembege, B., Tao, J. B., & Wang, S. (2008). Perpendicular electric field in two-dimensional electron phaseholes: A parameter study. *Journal of Geophysical Research*, *113*, A11219. https://doi.org/10.1029/2008JA013693

Lu, Q. M., Lu, S., Huang, C., Wu, M. Y., & Wang, S. (2013). Self-reinforcing process of the reconnection electric field in the electron diffusion region and onset of collisionless magnetic reconnection. *Plasma Physics and Controlled Fusion*, *55*(8). https://doi.org/10.1088/0741-3335/55/8/085019

Lu, Q. M., Wang, D. Y., & Wang, S. (2005). Generation mechanism of electrostatic solitary waves in the Earth's auroral region. *Journal of Geophysical Research: Space Physics*, *110*, A03223. https://doi.org/10.1029/2004JA010739

Lu, S., Lu, Q., Huang, C., & Wang, S. (2013). The transfer between electron bulk kinetic energy and thermal energy in collisionless magnetic reconnection. *Physics of Plasmas*, *20*(6), 061203. https://doi.org/10.1063/1.4811119

Matsumoto, H., Deng, X. H., Kojima, H., & Anderson, R. R. (2003). Observation of Electrostatic Solitary Waves associated with reconnection on the dayside magnetopause boundary. *Geophysical Research Letters*, *30*(6), 1326. https://doi.org/10.1029/2002GL016319

Mozer, F. S., Agapitov, O. V., Artemyev, A., Drake, J. F., Krasnoselskikh, V., Lejosne, S., & Vasko, I. (2015). Time domain structures: What and where they are, what they do, and how they are made. *Geophysical Research Letters*, *42*, 3627–3638. https://doi.org/10.1002/2015GL063946

Nakamura, R., Genestreti, K. J., Nakamura, T., Baumjohann, W., Varsani, A., Nagai, T., et al. (2019). Structure of the current sheet in the 11 July 2017 electron diffusion region event. *Journal of Geophysical Research: Space Physics*, *124*, 1173–1186. https://doi.org/10.1029/2018JA026028

Omura, Y., Matsumoto, H., Miyake, T., & Kojima, H. (1996). Electron beam instabilities as generation mechanism of electrostatic solitary waves in the magnetotail. *Journal of Geophysical Research*, *101*(A2), 2685–2697. https://doi.org/10.1029/95JA03145

Parker, E. N. (1957). Sweet's mechanism for merging magnetic fields in conducting fluids. *Journal of Geophysical Research*, *62*(4), 509–520. https://doi.org/10.1029/jz062i004p00509

Pollock, C., Moore, T., Jacques, A., Burch, J., Gliese, U., Saito, Y., et al. (2016). Fast plasma investigation for magnetospheric multiscale. *Space Science Reviews*, *199*(1–4), 331–406. https://doi.org/10.1007/s11214-016-0245-4

Pritchett, P. L. (2001). Geospace environment modeling magnetic reconnection challenge: Simulations with a full particle electromagnetic code. *Journal of Geophysical Research*, *106*(A3), 3783–3798. https://doi.org/10.1029/1999ja001006

Russell, C. T., Anderson, B. J., Baumjohann, W., Bromund, K. R., Dearborn, D., Fischer, D., et al. (2016). The magnetospheric multiscale magnetometers. *Space Science Reviews*, *199*(1–4), 189–256. https://doi.org/10.1007/s11214-014-0057-3

Shay, M. A., Drake, J. F., Rogers, B. N., & Denton, R. E. (2001). Alfvénic collisionless magnetic reconnection and the Hall term. *Journal of Geophysical Research*, *106*(A3), 3759–3772. https://doi.org/10.1029/1999ja001007

Sonnerup, B. U. Ö. (1979). Magnetic field reconnection. In L. T. Lanzerotti, C. F. Kennel, & E. N. Parker (Eds.), *Solar system plasma physics* (pp. 45–108). North-Holland.

Sonnerup, B. U. Ö., & Scheible, M. (1998). Minimum and maximum variance analysis. In G. Paschmann, & P. W. Daly, (Eds.), *Analysis methods for multi spacecraft data* (pp. 185–215). European Space Agency.

Steinvall, K., Khotyaintsev, Y. V., Graham, D. B., Vaivads, A., Contel, O. L., & Russell, C. T. (2019). Observations of electromagnetic electron holes and evidence of Cherenkov whistler emission. *Physical Review Letters*, *123*(25), 255101. https://doi.org/10.1103/PhysRevLett.123.255101

Steinvall, K., Khotyaintsev, Y. V., Graham, D. B., Vaivads, A., Lindqvist, P.-A., Russell, C. T., & Burch, J. L. (2019). Multispacecraft analysis of electron holes. *Geophysical Research Letters*, *46*, 55–63. https://doi.org/10.1029/2018GL080757

Sweet, P. (1958). *Electromagnetic phenomena in cosmical physics*. (123–134). Cambridge University Press.

Tong, Y., Vasko, I., Mozer, F. S., Bale, S. D., Roth, I., Artemyev, A., & Torbert, R. B. (2018). Simultaneous multispacecraft probing of electron phase space holes. *Geophysical Research Letters*, *45*, 11513–11519. https://doi.org/10.1029/2018GL079044

Torbert, R. B., Burch, J. L., Phan, T. D., Hesse, M., Argall, M., Shuster, R. J., et al. (2018). Electron-scale dynamics of the diffusion region during symmetric magnetic reconnection in space. *Science*, *362*(6421), 1391–1395. https://doi.org/10.1126/science.aat2998

Vaivads, A., André, M., Buchert, S. C., Wahlund, J.-E., Fazakerley, A. N., & Cornilleau-Wehrlin, N. (2004). Cluster observations of lower hybrid turbulence within thin layers at the magnetopause. *Geophysical Research Letters*, *31*(3). https://doi.org/10.1029/2003gl018142

Vaivads, A., Khotyaintsev, Y., André, M., Retinò, A., Buchert, S., Rogers, B., et al. (2004). Structure of the magnetic reconnection diffusion region from four-spacecraft observations. *Physical Review Letters*, *93*(10), 105001. https://doi.org/10.1103/physrevlett.93.105001

Vasko, I. Y., Agapitov, O. V., Mozer, F. S., Artemyev, A. V., Krasnoselskikh, V. V., & Bonnell, J. W. (2017). Diffusive scattering of electrons by electron holes around injection fronts. *Journal of Geophysical Research: Space Physics*, *122*, 3163–3182. https://doi.org/10.1002/2016JA023337

Vasyliunas, V. M. (1975). Theoretical models of magnetic field line merging. *Reviews of Geophysics*, *13*(1), 303–336. https://doi.org/10.1029/RG013i001p00303

Wang, R., Du, A., Nakamura, R., Lu, Q., Khotyaintsev, Y. V., Volwerk, M., et al. (2013). Observation of multiple sub-cavities adjacent to single separatrix. *Geophysical Research Letters*, *40*, 2511–2517. https://doi.org/10.1002/grl.50537

Wang, R., Lu, Q., Khotyaintsev, Y. V., Volwerk, M., Du, A., Nakamura, R., et al. (2014). Observation of double layer in the separatrix region during magnetic reconnection. *Geophysical Research Letters*, *41*, 4851–4858. https://doi.org/10.1002/2014GL061157

Wang, R. S., Lu, Q. M., Huang, C., & Wang, S. (2010). Multispacecraft observation of electron pitch angle distributions in magnetotail reconnection. *Journal of Geophysical Research*, *115*, A01209. https://doi.org/10.1029/2009JA014553

Wang, S., & Lu, Q. M. (2019). *Collisionless magnetic reconnection*. Science Publishing.

Wilder, F. D., Ergun, R. E., Goodrich, K. A., Goldman, M. V., Newman, D. L., Malaspina, D. M., et al. (2016). Observations of whistler mode waves with nonlinear parallel electric fields near the dayside magnetic reconnection separatrix by the magnetospheric multiscale mission. *Geophysical Research Letters*, *43*, 5909–5917. https://doi.org/10.1002/2016GL069473

Wu, M., Lu, Q., Huang, C., & Wang, S. (2010). Transverse instability and perpendicular electric field in two-dimensional electron phase-space holes. *Journal of Geophysical Research*, *115*, A10245. https://doi.org/10.1029/2009JA015235